Rocket system recovery using rotative wings

João Pedro Caldeira de Sousa Marques
joaopedrocaldeira@tecnico.ulisboa.pt

Instituto Superior Técnico, Universidade de Lisboa, Portugal

November 2022

Abstract

In this work, the feasibility of spacecraft recovery using rotative wings is analysed. This technology is based on the autorotation phenomenon, in which the rotor is driven without power associated. It possesses the ability to perform a safe and controlled landing, allowing the spacecraft to be reused and utilised in missions with different requirements. To fulfill the objective, a computational model that simulates the descent of a rocket's first stage was developed. It is based on rotor's aerodynamic theories and kinematics and computes several rotor parameters that allow the analysis of the system's performance. Moreover, it resorts to experimental data to increase the results' accuracy. The model's verification was successfully carried out by comparing its behaviour with literature data. The studies considered the recovery of an existing sounding rocket. To understand how each design parameter influences the system, a parametric study of the rotor design variables was held. It was concluded that the blade's pitch angle is extremely important for the system's performance and should be carefully selected, and that weight penalties resultant from excessive blade's number or radius can be prejudicial. Furthermore, a design optimisation was conducted, aiming to minimise the rocket's terminal velocity. The optimised solution decreased the terminal velocity by 72.7%, in comparison to the initial velocity. Finally, a flare manoeuvre was disclosed to reduce the touchdown velocity, resulting in a terminal velocity of 3.89 m/s. This recovery system is concluded to be highly promising, though requiring further work in several fields of study.
Keywords: Rocket Recovery Systems, Autorotation Dynamics, Rotative Wings, Autorotation Recovery Systems, Recovery System Design Optimisation

1. Introduction

Recovery of spacecrafts has always played an important role in space missions [1]. In the past decade, the space industry has been increasingly shifting towards commercialisation and searching for solutions that can make the enterprises economically sustainable. Recovering and reusing a spacecraft reduces massively the operational launch cost, allowing for more launches per year and thus a higher number of missions [2], offering a great solution to the problem.

The most common method of recovery is the parachute, which is reliable and able to decelerate a vehicle until a more or less soft landing [1]. However, the spacecraft's descent can not be piloted, neither its velocity can be changed [3]. Nowadays, the most successful technology is the autonomous vertical landing. In this method, the rocket has a controlled descent and is decelerated through its engines - meaning that it can be returned to Earth with a controlled trajectory and rate of descent and land softly and precisely, being reused.

The recovery using rotative wings is based on the autorotation phenomenon and is also able to perform a safe and controlled landing, allowing the spacecraft to be reused [3, 4]. Its advantage is that it brings a greater flexibility to the mission and possesses many applications [3, 4] - it has the potential, for instance, to be used for atmospheric research, since its flight path and velocity can be adjusted [4].

This technology was mainly considered in the second half of the last century. The main works in the field held analytical and experimental studies, such as the Kaman studies [4, 5] and the NASA Ames Research Center's program [6, 7], and provided interesting and promising results as for the spacecraft and rotor's performance. On the contrary, in the nineties, stability problems were obstacles for the development of Rotary Rocket Company's *Roton* [2]. Furthermore, recent studies cover the works of J. Hagen [3] and the ARMADA project [8, 9]. All the researchers revealed a great amount of confidence on the capabilities of such method, though with some doubts mainly regarding the system's stability.

Thus, the objective of this work is to address the feasibility of using a rotative wings system for the recovery of spacecraft. With this intention, a computational model was developed, offering the possibility to analyse the system's performance and culminating in a design optimisation in order to achieve a terminal velocity goal for a real situation.

2. Methods

This chapter describes the autorotation aerodynamic theory and the computational model developed. It also addresses the model's verification, by analysing an example and comparing it to the literature studies. Moreover, a mesh study is conducted.

2.1. Autorotation Aerodynamics in Axial Flight

Autorotation is a self-sustained phenomenon used to safely recover helicopters, more frequently in the event of an engine failure. It is, thus, an emergency state in which the vehicle's rotor remains on rotating and pro-

vides thrust, allowing the pilot to reduce the descent's velocity until a safe touchdown. It can be put into simple terms by the conservation of energy. During the descent, the vehicle gives up potential energy and the relative vertical descent velocity causes an upward airflow in the plane of the rotor, providing it with kinetic energy [10]. Eventually, the system reaches a steady state operation - the rotor's thrust equals the vehicle's weight, $T = W = mg$, the rotor torque becomes $Q = 0\ N \cdot m$ and the vehicle reaches a terminal velocity [10].

The aerodynamics of this phenomenon will now be explained resorting to the Blade Element Theory (BET) [10], assuming axial (vertical) flight. Figure 1 is a scheme of the airflow in an infinitesimal blade section [10]. The coordinate system is centred in the blade's root, so the positive x-axis is directed to the blade's tip. Since the vehicle is in a vertical descent, the resultant velocity relative to the rotor blades can be separated into two components: vertical, $\vec{U}_P$, and horizontal, $\vec{U}_T$ [10]. The vertical component is given by

$$\vec{U}_P = (V_c - v_i)\vec{e}_y = U_P\vec{e}_y \tag{1}$$

where $\vec{V}_c$ is the velocity vector of the airflow relative to the vehicle, caused by the air being forced up through the rotor (positive on the y-axis), and $\vec{v_i}$ is the axial induced velocity (negative on the y-axis), both in m/s [10]. These velocities are assumed to be uniform along the blade [10].

The horizontal component (parallel to the rotor and negative on the z-axis) at a particular blade section results from the blades rotative motion and is equal to

$$\vec{U}_T = \vec{\omega} \times \vec{x} = -\omega x\vec{e}_z = -U_T\vec{e}_z \tag{2}$$

in which $\vec{\omega}$ is the angular velocity vector of the rotor in rad/s and $\vec{x}$ is the x-coordinate vector of the section in m, with $0 \leq |\vec{x}| \leq R$, in which R is the radius of the blade, as observed in figure 2 [10].

The resultant velocity at one blade element is the sum of the two velocity vectors:

$$\vec{U} = U_P\vec{e}_y - U_T\vec{e}_z \tag{3}$$

The angle between $\vec{U}$ and the reference plane of the rotor is called induced angle of attack [10] and is given in degrees by

$$\phi = \tan^{-1}\left(\frac{\|\vec{U}_P\|}{\|\vec{U}_T\|}\right) \tag{4}$$

In addition, the pitch angle of the blades, θ, is the angle at which the rotor blades are set with respect to the plane of rotation [10], and will be assumed to be constant and equal through the blade (collective pitch). In figure 1, this angle is represented as being positive (airfoil leading edge pointing up) but, in an autorotative descent, it should have a negative value for the airfoil to generate the required forces to accelerate the rotor. Finally, the angle of attack of the airfoil, which is the angle between $\vec{U}$ and the airfoil's chord line, is

$$\alpha = \phi + \theta \tag{5}$$

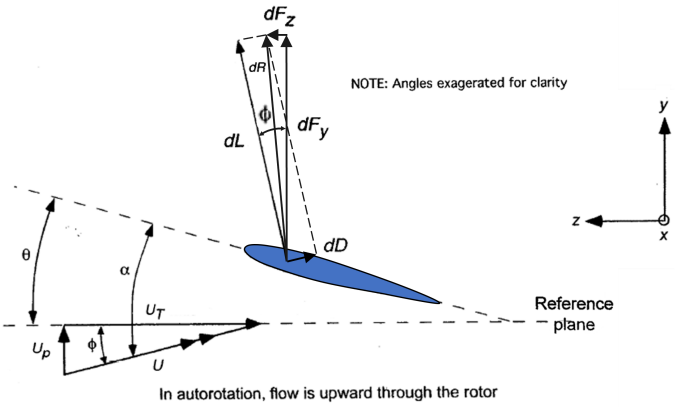

Figure 1: Side view of a blade element in autorotation, in axial flight. Adapted from [10].

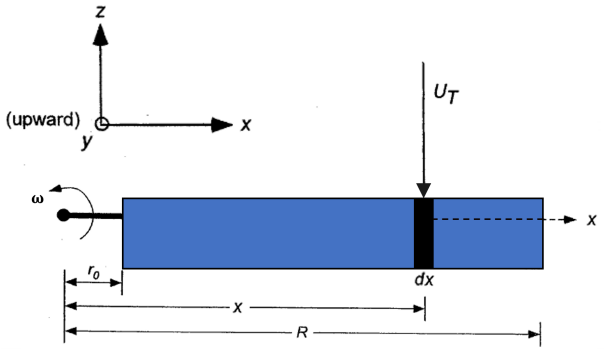

Figure 2: Top view of a blade element in autorotation, in axial flight. Adapted from [10].

The airflow creates lift, L, which is normal to the airflow direction, and drag, D, which is parallel [10]. Therefore, for each blade element, one has, in N,

$$\|d\vec{L}\| = \frac{1}{2}\rho\|\vec{U}\|^2 cC_l dx \tag{6}$$

$$\|d\vec{D}\| = \frac{1}{2}\rho\|\vec{U}\|^2 cC_d dx \tag{7}$$

where C_l and C_d are the lift and drag coefficients, respectively, ρ is the density of the air in kg/m^3, dx is the length of each blade element, in m, and c is the local blade chord of the blade, also in m [10]. In this work, the blades are assumed to have a rectangular shape, what means that c is constant throughout the blade's span.

The addition of $d\vec{L}$ and $d\vec{D}$ is a resultant force vector $d\vec{F}_{res}$ that can be decomposed into: a vertical component $d\vec{F}_y$ that provides an upwards force, decelerating the vehicle's descent; a horizontal component $d\vec{F}_z$, parallel to the rotor disk plane, that provides the blades with rotary motion. These forces contribute, respectively, to the rotor's infinitesimal thrust, in N, and torque, $N \cdot m$, equal to

$$d\vec{T} = N_b\Big(\|d\vec{L}\|\cos\phi + \|d\vec{D}\|\sin\phi\Big)\vec{e}_y = dT\vec{e}_y \tag{8}$$

$$d\vec{Q} = N_b\Big(\|d\vec{L}\|\sin\phi - \|d\vec{D}\|\cos\phi\Big)x\vec{e}_y = dQ\vec{e}_y \tag{9}$$

where N_b is the number of blades of the rotor. Note that the latter expressions are only valid for axial flight, since the aerodynamic environment is assumed to be axisymmetric (uniform in all the points of the rotor) [10].

Finally, according to the BET [10], dT and dQ can be integrated across the blade's span to obtain the total rotor's T and Q. This integration is of considerable difficulty of resolution, given to the fact that at each blade element U_T changes with the x-coordinate of the section (see equation 2), increasing from 0 m/s at $x = 0\ m$ (root) until its maximum value at $x = R$ (tip). Consequently, both $\vec{U}$ and ϕ will vary across the blade, what varies α, C_l and C_d. For this reason, all the referred parameters depend on the x-coordinate, making the analytical calculation of the T and Q of the rotor challenging. Thus, an approximation was made and $\vec{T}$ and $\vec{Q}$ are obtained by summing the contributions of each blade element:

$$\vec{T} = \sum_{j=1}^{n_{\text{sections}}} d\vec{T}_j \tag{10}$$

$$\vec{Q} = \sum_{j=1}^{n_{\text{sections}}} d\vec{Q}_j \tag{11}$$

where $n_{\text{sections}} = R/dx$ is the number of sections in a blade.

In addition, the fact that α varies along the blade brings other implications. As known, variations of α are related to variations of C_l and C_d, and when α surpasses the critical angle of attack (value of α corresponding to the highest C_l value), α_{crit}, the airfoil stalls due to the separation of the boundary layer from the airfoil, resulting in a loss of L.

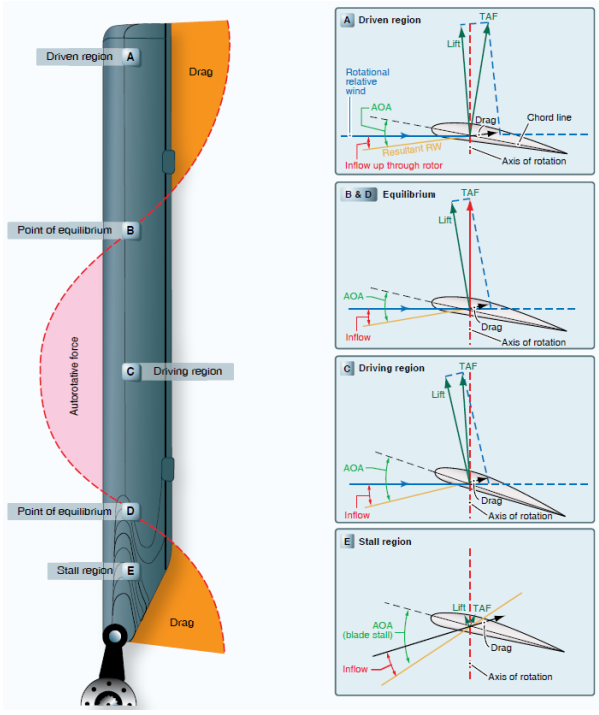

Figure 3: Blade regions and respective aerodynamic forces, for an axial autorotative descent [11].

Since C_l and C_d are different across the blade's span, one can comprehend that the steady autorotative condition of $\|d\vec{Q}\| \approx 0\ N \cdot m$ is not verified for each blade section (see equation 9) [10]. For this reason, certain stations of the rotor will absorb power from the airflow, while others will dissipate it [10]. Nevertheless, this phenomenon results in the sum of the several $d\vec{Q}$'s to be $\int \|d\vec{Q}\| \approx 0\ N \cdot m$, complying with the steady autorotative condition [10]. The stated phenomenon will then form either two or three different zones in the rotor disk: the driven region, the driving region and, possibly, the stall region. The zones are showed in figure 3 and represented as letters.

The driven region (A) is located near the blade's tip and accounts for about 30% of the blade's radius [11]. The value of U_T on this zone is at its highest, resulting in a low ϕ and, consequently, in a low α. Thus, the horizontal component of $\|d\vec{L}\|$ can not overcome the profile drag, meaning that the horizontal component of $d\vec{F}_{res}$ has the opposite direction to the rotation direction of the blades, decelerating its rotation - the driven region dissipates energy. Nonetheless, this resulting force also produces T.

There are two equilibrium points between the driven and driving regions (B) and between the driving and stall regions (D), in which $d\vec{F}_{res}$ only has a vertical component. Hence the resulting force only produces T and not Q.

Moving to the centre of the rotor, there is the driving region (C). In this region, U_T is smaller than in region A, which results in higher α's. The horizontal component of the lift overcomes the profile drag, producing the necessary force to keep the blades turning. Thus, this region absorbs power from the airstream to the rotor, accelerating the rotation of the blades. It consists of about 25 to 70% of the blade's radius [11].

Finally, near the root there is the stall region (E), consisting of the blade's remaining 25% [11]. In this region, U_T decreases and α increases (possibly until values close to 90°), becoming higher than α_{crit}. The airfoil is then stalled and drag is produced, decelerating the blades.

By controlling the size of the regions, Q and therefore ω can be controlled. This is achieved by varying θ, which significantly affects the aerodynamic forces and moments [7]. Concluding, for achieving a constant ω, θ must be adjusted to a point in which the accelerating moment provoked by the driving region equals the decelerating moment caused by the driven and stall regions.

2.2. Computational Model

In this work, a computational model of the recovery of a rocket's first stage was developed. The model's foundations are based on a simple model developed by Amato et al. [12], and it simulates the axial descent of a spacecraft with rotative wings, resorting to the BET and kinematic equations. Figure 4 shows the coordinate system of the rocket's body. An important approximation is that the body's y-axis is always oriented normally to the Earth's surface and that no movement is considered on the x and z-axis. In addition, all the forces are assumed to be applied on the body's centre of mass and no moments are to be produced, except for Q, which is applied on the rotor.

The flight begins with a vertical freefall during a spec-

ified period of time, t_{deploy}, until the rotor's deployment. The body initiates the descent at a specific height (vertical distance between the vehicle and the soil, in m), h_0, with no vertical velocity, $v_{v_0} = 0\ m/s$ (velocity of the airflow in relation to the body, being equivalent to its descent velocity), and an acceleration that is equal to the gravitational acceleration, $a_{v_0} = -g$. The freefall simulates the first stage's descent after its separation from the rocket and induces a non-null initial vertical velocity at the moment of the rotor's deployment. When the rotor is deployed its angular velocity, ω_0, and angular acceleration, a_{ang_0}, are also assumed as null.

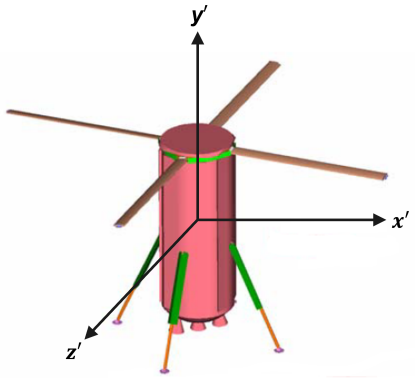

Figure 4: Coordinate system of the first stage's body. Adapted from [3].

Other simulation's initial variables include the first stage's length, Lt_{stage}, and diameter, Dm_{stage}, both in m (the first stage is approximated as a cylinder), and its mass, m_{stage}, in kg. As for the rotor, the design variables are N_b, R, c and θ.

In addition, other rotor's design parameters are calculated. The rotor's solidity, σ, and disk loading, DL in kg/m^2, are respectively given by

$$\sigma = \frac{N_b A_b}{A_{disk}} = \frac{N_b R c}{\pi R^2} = \frac{N_b c}{\pi R} \tag{12}$$

$$DL = \frac{m}{A_{disk}} = \frac{m}{\pi R^2} \tag{13}$$

in which A_b is the area of a blade and A_{disk} is the area of the rotor's disk, both in m^2, and m is the total mass of the system (first stage plus recovery system). The recovery system's mass, $m_{recovery}$, estimated from [8], increases with N_b and R.

The freefall is based on kinematic motion equations and computed through an iterative process, calculating the successive heights, h, vertical velocity vector, $\vec{v}_v$, and acceleration vector, $\vec{a}_v$, of the body. The time of the simulation t is also continuously iterated with an increment of dt. During this freefall, $\vec{a}_v$ becomes dependent on the vertical drag force of the first stage, $\vec{D}_{stage}$, which is positive on the y-axis of figure 4, and equal to

$$\vec{D}_{stage} = \left(\frac{1}{2}\rho C_{d_{stage}} \|\vec{v}_v\| A_{base}\right)\vec{e}_{y'} \tag{14}$$

in which $C_{d_{stage}}$ is the cylinder's axial drag coefficient and A_{base} is the reference area, in this case of the cylinder's base. To calculate $C_{d_{stage}}$, experimental values of Computational Fluid Dynamics (CFD) simulations [13] were inputted in the model, and this coefficient depends only on the cylinder's aspect ratio, $AR = (Lt/Dm)_{stage}$.

Apart from this, an enhancement was made to the program: for each iteration, atmospheric parameters such as ρ and temperature Tp, in K, are successively computed for each h, being inputted from empirical models, to increase the accuracy of the results. In the same manner, g and the dynamic viscosity of the air μ, in $kg/(m \cdot s)$, are also updated resorting to the law of universal gravitation and to the Sutherland's Law, respectively.

When $t = t_{deploy}$, the rotor is deployed and the BET equations are used to calculate the forces generated, throughout an iterative process that terminates when $h = 0\ m$. The rotor is assumed to be instantly deployed.

Following deployment, the airflow induces the generation of forces on the blades. Since such forces are distinct along the blade, the model divides the blade in $n_{sections}$ sections and successively calculates the infinitesimal forces on each one through an iterative process, resorting to the equations described in section 2.1.

Equations 6 and 7 involve C_l and C_d, which depend on α and on the Reynolds number, Re. The Re at each blade element is equal to

$$Re = \frac{\rho \|\vec{U}\| c}{\mu} \tag{15}$$

In the model that served as a basis for this work's model [12], the computation of these coefficients was quite inaccurate and deceptive, so an alternative approach was taken. It consisted in creating a database of C_l and C_d as a function of α, for a wide range of Re numbers. For α's below α_{crit}, computational data obtained from simulations in the aerodynamic software XFLR5® is used. Above α_{crit}, this software fails to compute trustworthy values due to the separation of the boundary layer [14], and the situation is more challenging since values for α up to 90° are necessary. It is seen that, following the C_l loss due to stall, there is a recovery of this value and for a higher α it eventually becomes independent of Re. This means that, above the referred α, experimental data of wind tunnel testing for a single Re can be used, from [15]. Nevertheless, between α_{crit} and the α at which the coefficients become independent of Re, there is still a considerable dependence on Re. Thus, in order to consider this dependence but not excessively jeopardise the results, the solution was to resort both to the computational and the experimental data for this range, with a weighting being made. Until α_{crit}, only the XFLR5® data is used - the computational data has a weight of 100%. Between α_{crit} and the referred α, the weight of the XFLR5® data is progressively decreased with increasing α, while the experimental data's weight is increased. Finally, above that α, the experimental data has a weight of 100%. This was the best way to compute several plots of C_l and C_d depending on α, for a wide Re number range.

With C_l and C_d, the calculations for each blade section are completed and eventually T and Q are obtained. Thus, T will influence a_v and consequently v_v and h for the next iteration, that become

$$\vec{a}_v = \left[\left(\frac{T + D_{stage}}{m}\right) - g\right]\vec{e}_{y'} \tag{16}$$

$$\vec{v}_v = (v_{v_0} - a_v dt)\,\vec{e}_{y'} \tag{17}$$

$$h = h_0 - \|\vec{v}_v\|\,dt + \frac{1}{2}\|\vec{a}_v\|\,dt^2 \tag{18}$$

while Q has an influence on a_{ang} and ω, which are given by

$$\vec{a}_{ang} = \frac{Q}{I_{rotor}}\vec{e}_y \tag{19}$$

$$\vec{\omega} = (\omega_0 + a_{ang} dt)\,\vec{e}_y \tag{20}$$

in which I_{rotor} is computed by assuming that the rotor is only composed by the blades and that these are approximated as thin rectangular plates. Its value increases with R, c and with the rotor's mass.

Finally, other parameters for rotor's performance analysis are computed. The rotor drag coefficient, C_{d_R}, is given by

$$C_{d_R} = \frac{T}{\frac{1}{2}\rho {U_P}^2 A_{disk}} \tag{21}$$

and the axial advance ratio, λ_{axial}, is equal to

$$\lambda_{axial} = \frac{U_P}{V_{tip}} = \frac{U_P}{\omega R} \tag{22}$$

where V_{tip} is the velocity of the blade's tip [10]. Following the calculations, the described process restarts.

2.2.1 Axial Induced Velocity in Axial Flight

In equation 1, U_P depends on v_i. The latter is used to compute the inflow through the rotor (negative on the y-axis of figure 1) and should be taken into account to assure the model's reliability, since it alters the vertical velocity of the airflow on the blades. Such parameter was also not considered in the base model [12]. To obtain it, the momentum theory in axial flight is put into practice [10] and the velocity in a state of hover, v_h, must be calculated:

$$v_h = \sqrt{\frac{W}{2\rho A_{disk}}} = \sqrt{\frac{mg}{2\rho\pi R^2}} \tag{23}$$

For the momentum theory to be applied, the condition of the windmill brake state, $V_c > 2v_h$, should be complied with. In this operation mode, v_i is

$$v_i = v_h\left(\frac{V_c}{2v_h} - \sqrt{\left(\frac{V_c}{2v_h}\right)^2 - 1}\right) \tag{24}$$

For $0 \leq V_c \leq 2v_h$, the rotor operates in the vortex ring state, in which the momentum theory is invalid due to unstable flow. However, if necessary, it is possible to resort to empirical data in order to obtain v_i, without considering the unstable and turbulent effects [10].

From equation 24, the value of v_i depends on V_c for the current iteration, and V_c is obtained through the forces in the rotor, which in turn depend on U_P, that depends on v_i. Thus, it was necessary to implement one more iterative process for the convergence of U_P.

2.2.2 Model Verification

The verification of the model was conducted by focusing on the behaviour of the problem's physical variables, and by providing qualitative comparisons with the literature, since no quantitative comparisons were possible.

In this part of the work, there is a freefall of $t_{deploy} = 3.09\ s$. It was then observed that the plots of both a_v and a_{ang}, seen in figures 5(a) and 5(b), present two peaks. The first a_v peak occurs since the blades act similarly to flat plate drag surfaces, which means that they are fully stalled. The second peaks are justified by the fact that the rotor transitioned from being fully stalled to being only partially stalled. These peaks result in a decrease of v_v and an increase of ω. Moreover, the behaviour of T and Q is the same as a_v and a_{ang}, respectively.

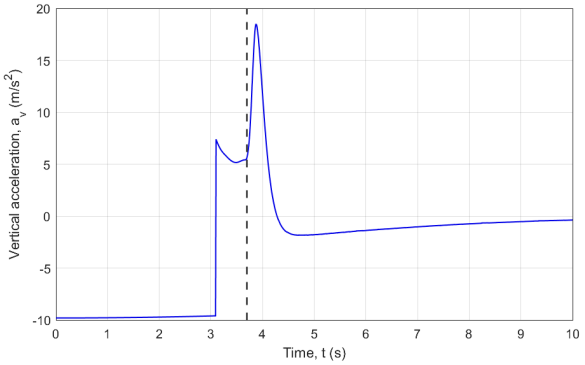

(a)

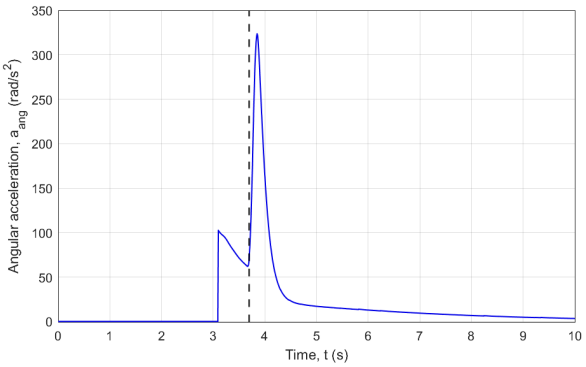

(b)

Figure 5: Evolution of a_v (a) and a_{ang} (b) with t, with the second acceleration peak highlighted.

To better justify the occurrence of the second peak, the spanwise distribution of the blade's α was analysed in three different instants. It was concluded that, between the first and second peaks, 100% of the blade is stalled, while at the maximum value of a_v registered, this value drops and the blade becomes partially stalled. In the end of the simulation, in equilibrium, this value is only of about 30%. This was confirmed by [16].

Accordingly, the evolution of C_{d_R} with λ_{axial} confirmed the previously stated. References [4, 5] claim that the blades are partially stalled for $\lambda_{axial} < 0.5$, what can also be seen in figure 6. In fact, around this value of λ_{axial}, C_{d_R} increases substantially, and this was observed to occur approximately when a_v begins to rise again.

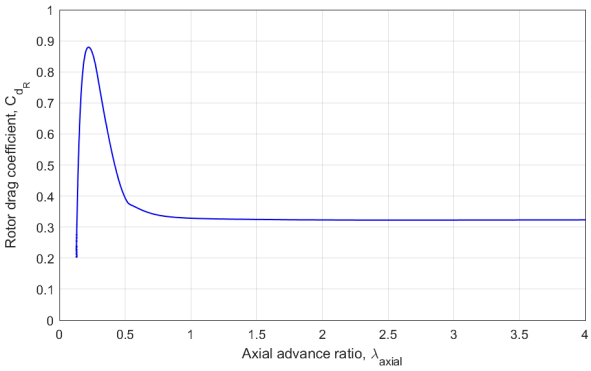

Figure 6: C_{d_R} variation with λ_{axial}.

Following the peaks, a_v and a_{ang} (or T and Q, respectively) eventually reach a near steady state operation, or autorotation, as described in section 2.1. In this moment, the spanwise distribution of the blade's dQ was also analysed (see figure 7), verifying the three zones presented in section 2.1 and being confirmed by [16].

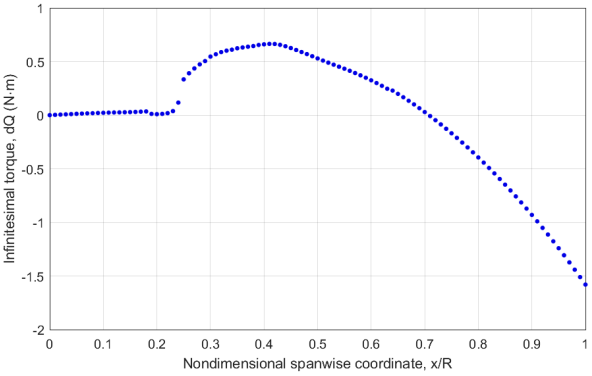

Figure 7: Spanwise distribution of the dQ of a blade's section in autorotation.

The terminal values were close to the equilibrium values expected, with the differences obtained being justified by numerical errors and approximations.

2.2.3 Mesh Study

In order to guarantee the reliability of the results obtained, a mesh study of dx and dt was held. These parameters were studied separately, considering an extremely low value of each as a reference, since the latter culminate in more trustworthy results but also on a higher computational time. It was decided that $dx = 0.1$ m and $dt = 0.1$ s were satisfying selections, even though it is mandatory to select $dt = 0.01$ s or lower whenever the model considers v_i, for convergence purposes.

3. Computational Experiments

In this chapter, a real situation is addressed, in order to comprehend the performance of the recovery system, as well as its feasibility. A parametric design study, a design optimisation and the demonstration of a touchdown manoeuvre are conducted.

3.1. *Baltasar* Sounding Rocket

The selected scenario was the recovery of the sounding rocket *Baltasar* [17], with a touchdown velocity goal of around 5.95 m/s. It reaches an altitude of about $3,000$ m, having a freefall of $t_{deploy} = 3.09$ s. When the rotor is deployed, one has $h_{deploy} \approx 2,976$ m and $v_{v_{deploy}} \approx 30$ m/s. These are real values provided to the author, allowing to fix the initial kinematic conditions and leaving room to focus on studying the recovery system itself.

3.2. Parametric Study

This study involves the analysis of the following design parameters: R, N_b, and θ. It consists in investigating how the system's performance varies with the change of each design variable, with an emphasis on minimising the terminal v_v. The mesh parameters used were based on the mesh study conducted.

3.2.1 Variation of R

Regarding variations of blade's R, the values were in the range of $R = 0.4$ m to $R = 3$ m. Figures 8(a) and 8(b) show the variation of v_v and a_v with t for the several studied R's. All the plots follow the same tendency, with the exception of $R = 0.4$ m and $R = 3$ m.

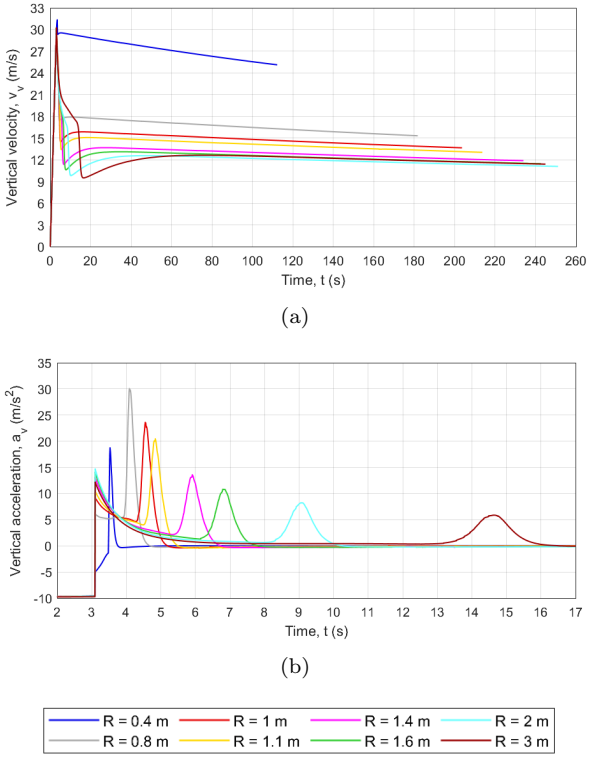

Figure 8: Evolution of v_v (a) and a_v (b) with t, for the several R's studied.

Excluding these two values, it is generally observed that lower terminal v_v's occur for higher R's. Additionally, the first peak of a_v is higher with increasing R, while the second one is lower. Furthermore, increasing R "delays" the transition of the blades to a partially stalled operation, since the second peak occurs later, what was seen to result in lower terminal v_v's. It is also observed that, as R increases, the differences on the curves of v_v become smaller, converging to a certain terminal v_v.

The main findings from this study were that $R = 0.4$ m is not sufficient for the blades to have a positive first a_v peak, not being able to adequately decelerate the system. Contrarily, $R = 3$ m is an excessive value, since the terminal v_v is higher than the one obtained for $R = 2$

m. For $R = 3\ m$, both a_v peaks are lower then the ones for $R = 2\ m$ even though its T is higher, given to the fact that $R = 3\ m$ results in an excessive $m_{recovery}$, prejudicing the system's performance (see equation 16).

As for the rotor, a higher R results in lower a_{ang}'s and ω's due to a higher I_{rotor}, even though Q increases with R (equation 19). The successively lower equilibrium ω's can be advantageous not to induce blade's overspeeding.

3.2.2 Variation of N_b

In the same manner, N_b between 2 and 5 was analysed. Since $m_{recovery}$ also increases with N_b, it would be expected that, at some point, the situation referred above would happen again. However, $N_b = 5$ actually delivered the best results. Generally, the same observations of the R study can be made for the N_b analysis, with a first peak of a_v being higher with increasing N_b, contrarily to the second peak. Additionally, increasing N_b also "delays" the blade's operational transition, resulting in lower terminal v_v's. Moreover, a_{ang} is lower with N_b, as is ω.

From equation 12, σ is directly proportional to N_b. References [4, 5] state that both the value of C_{d_R} and the value of λ_{axial} for which the maximum C_{d_R} occurs increase with σ, something that is registered in this study (see figure 9). However, these references predict the curves to be proportional to σ only for the region in which the blades are fully stalled ($\lambda_{axial} > 0.5$), something that was not observed herein, since the curves are nearly proportional to σ for the whole λ_{axial} range.

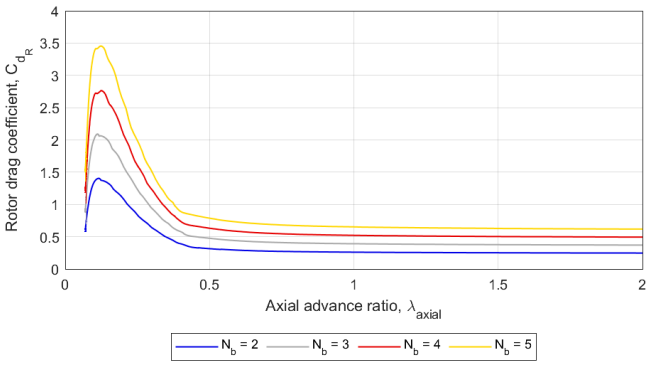

Figure 9: C_{d_R} variation with λ_{axial} for the several N_b's studied.

3.2.3 Variation of θ

Finally, the θ variation is studied, since it is the most defining parameter of the performance of an autorotative descent. For the blades to rotate in the right direction, all the selected values of θ were negative, between $\theta = -10°$ and $\theta = -2°$.

Figures 10(a) and 10(b) display the evolution of v_v and a_v with t for the θ range considered.

The first peak of a_v observed is higher with increasing θ (less negative), since the blades become closer to being perpendicular to the axial airflow, producing higher T's, but lower Q's.

The first conclusion taken is that the values of $\theta = -10°$ and $\theta = -5°$ are not efficient, because between the first and second peaks there is a period in which a_v is negative, which adversely increases v_v. This does not happen for the other θ's.

Regarding the second a_v peak, an important finding is that $\theta = -2.8°$ and $\theta = -2°$ do not possess one. Even though their first peaks are the highest, the blades are not capable of generating enough Q for ϕ (and α) to decrease significantly, meaning that the blades remain fully stalled, never overcoming this state. By analysing the spanwise distribution of the blade's α in equilibrium (see figure 11), for $\theta = -2°$, it became clear that the blade was completely stalled. These values were also considered as inefficient.

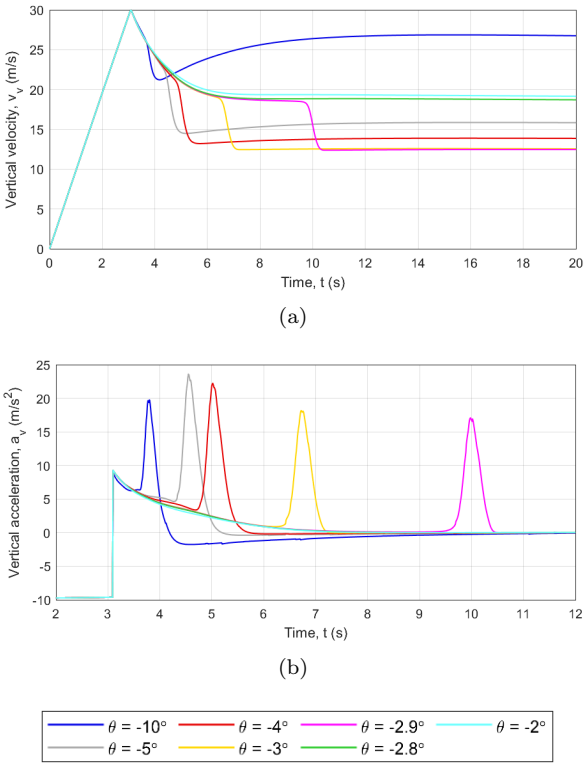

Figure 10: Evolution of v_v (a) and a_v (b) with t, for the several θ's studied.

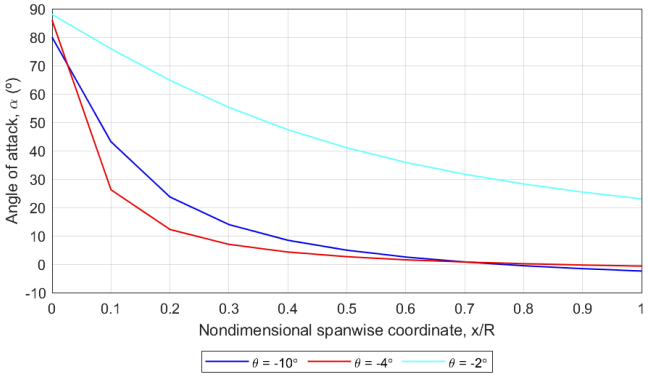

Figure 11: Spanwise distribution of the α of a blade's element for $\theta = -10°$, $\theta = -4°$ and $\theta = -2°$.

As for the remaining angles, the second peak is smaller with increasing θ (except for $\theta = -10°$) and occurs later. This means that the rotor "delays" the transition from fully stalled to partially stalled blades. As a matter of fact, it was observed that, especially for $\theta = -3°$ and $\theta = -2.9°$, the value of λ_{axial} remains constant at $\lambda_{axial} \approx$

0.4 for some seconds, dropping afterwards, moment at which the transition occurs and the peaks begin. This results in a lower terminal v_v. In addition, the spanwise distribution of the blade's α in equilibrium, of figure 11, showed that for $\theta = -10°$ approximately 30% of the blade is stalled, while for $\theta = -4°$ this percentage drops to less than 20%.

Furthermore, both a_{ang} peaks are higher for lower θ's (more negative), what results in higher ω's. This is justified by the fact that the reduction of θ increases the generation of Q.

Finally, the most efficient θ range for this specific design was assessed. Reference [8] states that this value is, from the θ's that induce an unstalled operation, the highest. Equivalently, reference [16] asserts that this angle is located between $\theta = 0°$ and θ for which the equilibrium dimensionless tip speed, $\Omega^* = 1/\lambda_{axial}$, is maximum. The plots of equilibrium Ω^* and C_{d_R} with θ can be seen in figures 12(a) and 12(b) and are in accordance with references [6] and [9]. The difference between an unstalled and stalled operation becomes evident, with the stalled operation being identified for $\theta > -2.9°$, denoted by a sudden decrease on the values of Ω^* and C_{d_R}, as seen for the case of $\theta = -2.8°$. On the contrary, for $\theta = -2.9°$ the blades are partially stalled, presenting the highest value of Ω^* and C_{d_R}.

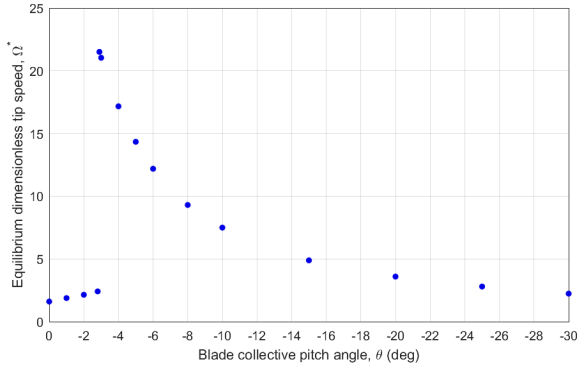

(a)

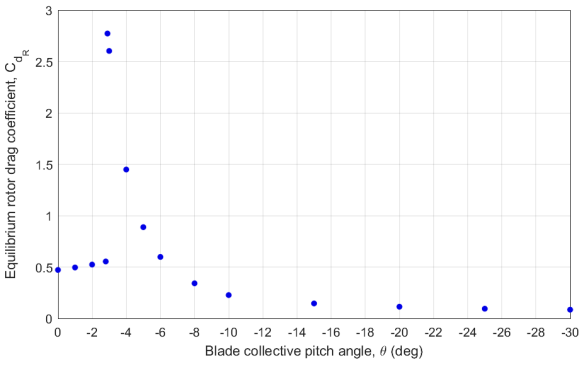

(b)

Figure 12: Variation of the equilibrium Ω^* (a) and C_{d_R} (b) with θ.

For this reason and taking into account that $\theta = -2.9°$ also demonstrated the best results as for terminal v_v, the model confirmed the predictions made by the literature studies. Thus, it was concluded that the most efficient θ is within the range $-2.9° \leq \theta < -2.8°$.

The θ parametric study resulted in the highest v_v reductions from the three parametric studies conducted, proving the importance of θ for the system.

3.3. Genetic Optimisation

Following the parametric study, a Genetic Optimisation (GA) was held to address the design that achieves the lowest terminal v_v. Thus, N_b, R, c and θ were selected as design variables and bound constraints were defined for each, taking into consideration the results obtained in the parametric study. The only objective function was v_v, which was intended to be minimised.

The optimised solution of the GA led to a design that displayed a terminal v_v of $v_v \approx 8.24\ m/s$, representing a decrease of 72.7% in comparison to $v_{v_{deploy}}$. The design variables that produced the minimised solution are seen in table 1. These values are within the best values observed in the parametric studies (for instance, $-2.9° \leq \theta < -2.8°$).

Table 1: Design variables that resulted in the optimised solution.

N_b	$R\ [m]$	$c\ [m]$	$\theta\ [°]$
4	1.9213	0.0926	−2.8123

3.4. Optimised Solution

The solution that achieved the best results (table 1) was then addressed. Figures 13, 14, 15 and 16 depict the evolution of v_v, a_v, ω and a_{ang} with t, for this simulation. As for a_v, a first peak with a maximum $a_v \approx 6.89\ m/s^2$ (approximately 0.70 g's) was seen, while a_{ang} had a maximum of $a_{ang} \approx 4.59\ rad/s^2$. Following the first peak, the model entered a state of near equilibrium in which both accelerations were approximately null.

As evidenced by the parametric analysis, a greater time interval between the two acceleration peaks was characteristic of designs that provided lower terminal v_v's. Such factor explains the interval of roughly 160 s ascertained between the two peaks. It was then confirmed that the minimised solution "delays" substantially the transition of the blades from fully stalled to partially stalled, as expected.

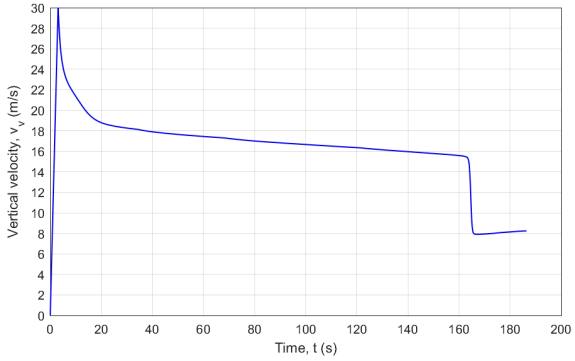

Figure 13: Variation of v_v with t for the GA solution.

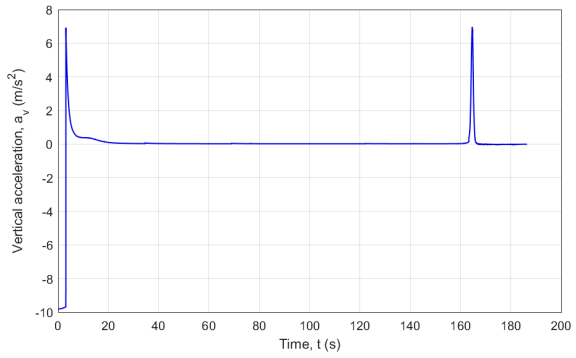

Figure 14: Variation of a_v with t for the GA solution.

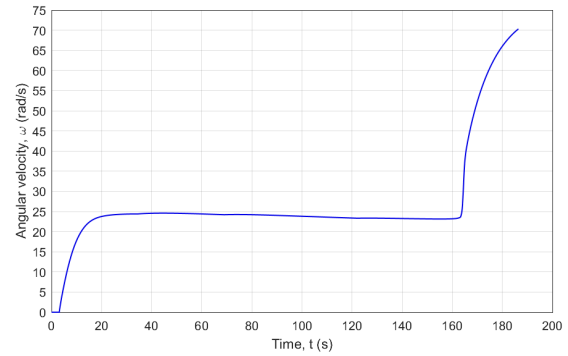

Figure 15: Variation of ω with t for the GA solution.

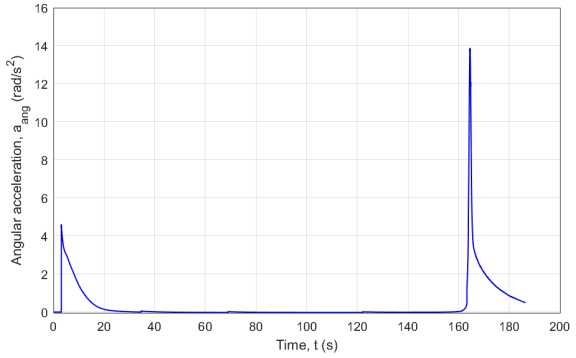

Figure 16: Variation of a_{ang} with t for the GA solution.

Furthermore, the second acceleration peak resulted in maximum values of $a_v \approx 6.94\ m/s^2$ (approximately 0.71 g's) and $a_{ang} \approx 13.86\ rad/s^2$, corresponding to a maximum of $T \approx 613.35\ N$ and $Q \approx 149.16\ N \cdot m$, respectively. This resulted in a decrease of v_v until a terminal $v_v \approx 8.24\ m/s$, and an increase of ω, which presented a value of $\omega \approx 70.31\ rad/s$ at $h = 0\ m$. This demonstrated the recovery system's promising deceleration capabilities. It was also evident that, since the second peak of acceleration occurred so late, there was not enough time for the system to reach an equilibrium state again - this becomes clear by looking at figure 16.

Looking at the spanwise distribution of dQ in the end of the simulation (not in equilibrium, though), the stall region was registered to be only of approximately 16% of the blade, denoting a great improvement in comparison to what was observed in figure 7.

Moreover, it was verified that, as observed in the N_b parametric study, the value of λ_{axial} for which the C_{d_R} variation becomes steeper is lower as the system becomes more efficient, in this case being $\lambda_{axial} \approx 0.33$ - the lowest value registered throughout all the studies. Finally, the maximum C_{d_R} was $C_{d_R} \approx 1.45$, while in the end of the simulation it was $C_{d_R} \approx 1.19$, which is a lower value than the expected C_d of the parachute designed by RED.

Consequently, it is understandable that this configuration did not fulfill the design goal of $v_v = 5.95\ m/s$.

3.4.1 Collective Flare Manoeuvre

A final study was held to both solve the latter problem and demonstrate the ability of performing a collective flare manoeuvre to further reduce the v_v at touchdown. Such manoeuvre is put into practice by collectively changing θ to induce blade's stall, acting as flat drag plates and producing a higher deceleration at touchdown [4]. The optimised solution was run again, with the difference that, when $h < 20\ m$, θ was varied to $\theta = 0°$. Since V_c decreases, at some point v_i had to be calculated by considering the rotor's operation in the vortex ring state (see subsection 2.2.1).

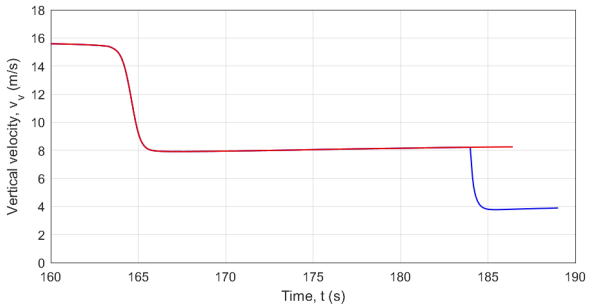

(a)

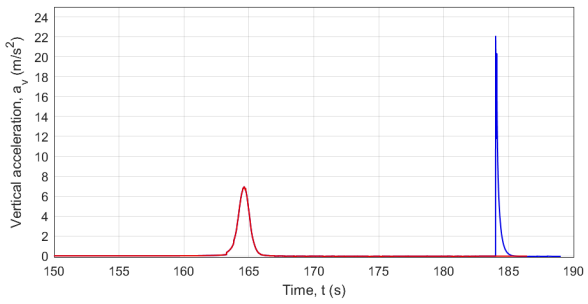

(b)

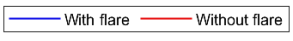

Figure 17: Variation of v_v (a) and a_v (b), with and without performing the collective flare manoeuvre.

The results obtained for v_v and a_v for the last seconds of the simulation are shown in figures 17(a) and 17(b), underlining the differences of resorting to the flare manoeuvre. As observed, v_v was decreased to a touchdown value of $v_v \approx 3.89\ m/s$, caused by a maximum a_v of approximately 2.24 g's. This value complies with the objective, representing a v_v decrease of 87.1% in comparison to $v_{v_{deploy}}$, and a decrease of 52.8% with regard to the terminal v_v without applying this manoeuvre. Thus, the mission would be successful regarding the terminal v_v requirement.

4. Conclusions

In this work, the feasibility of rotative wings for the recovery of spacecraft was investigated, assessing its potential in comparison to the most common recovery methods. It resulted in the conception of a bibliographical compendium, which proved useful for the subsequent parts of the work.

To carry out the viability analysis, a computational model that simulates the full descent of a rocket's first stage with a self-rotating rotor was developed. The model was successfully verified, being confirmed to have the same behaviour of an autorotating rotor through comparisons with literature studies.

A parametric study regarding the rotor's design parameters was held. It led mainly to the following conclusions: θ was seen to be the most defining parameter from the ones studied, and should be carefully selected in order to achieve the most efficient configuration (a non stalled one); increasing N_b or R results generally in a lower terminal v_v, but a too high value can be prejudicial due to the weight penalties associated; the more efficient the design, the more the transition from a blade's fully stalled operation to a partially stalled operation is "delayed", what leads to lower terminal v_v's. This study allowed to better comprehend the effects provoked on the system's performance by varying each design variable.

Following the parametric studies, a design optimisation was conducted, with the solution achieving a terminal $v_v \approx 8.24\ m/s$, which reflects on a decrease of 72.7% from the initial v_v value. Finally, the collective flare manoeuvre for touchdown was demonstrated so that the terminal v_v goal of $v_v = 5.95\ m/s$ was reached. This study was successful, with a total decrease of 87.1%, without considering the vortex ring state's unstable effects, though.

Concluding, this proof of concept confirmed that it is feasible to resort to rotative wings to safely recover a rocket's first stage, with regard to its terminal v_v, though with a number of approximations and assumptions. The rotative wings recovery system presents advantages that make it extremely interesting in comparison to the most commonly used systems, especially regarding its versatility, and shows potential. Nonetheless, and understandably, many other studies are still required, especially regarding stability, to fully address its feasibility.

References

[1] R. D. Launius and D. R. Jenkins. *Coming home: reentry and recovery from space (1st ed.)*. NASA, 2012.

[2] G. C. Hudson. Roton development and flight test program. In *AIAA Defense and Civil Space Programs Conference and Exhibit, AIAA 98-5258*, Huntsville, AL, U.S.A., October 1998.

[3] J. D. Hagen. Rotor Landing Technology for Crew Exploration Vehicle (CEV) Earth-to-Orbit Crew Transport. In *1st Space Exploration Conference: Continuing the Voyage of Discovery, AIAA 2055-2508*, 2005.

[4] Kaman Aircraft Corporation. *Investigation of Stored Rotors for Recovery*. Technical Documentary Report No. ASD-TDR-63-745, 1963.

[5] J. J. Barzda. Rotors for Recovery. In *AIAA Entry Technology Conference*, Williamsburg and Hampton, VA, U.S.A., 1964.

[6] A. D. Levin and R. C. Smith. *An analytical investigation of the aerodynamic and performance characteristics of an unpowered rotor entry vehicle*. NASA Ames Research Center, NASA TN D-4537, 1968.

[7] R. C. Smith and A. D. Levin. *Experimental Aerodynamic Performance Characteristics of a Rotor Entry Vehicle Configuration. 1 - Subsonic*. NASA TN D-7046, 1971.

[8] T. V. Peters, R. Cadenas, D. Modenini, P. Tortora, E. Kervendal and J. Kohler. ARMADA: Autorotation, feasible alternative to traditional Martian Entry, Descent and Landing. In *60th International Astronautical Congress*, 2009.

[9] D. Modenini, M. Zannoni and P. Tortora. Optimal Blade Pitch Profile for an Autorotative Entry Vehicle. *Advances in the Astronautical Sciences Series, Vol. 162*, page 765–776, 2018.

[10] J. G. Leishman. *Principles of helicopter aerodynamics (2nd ed.)*. Cambridge University Press, 2006.

[11] FAA. *Helicopter Flying Handbook: FAA-H-8083-21B*. Aviation Supplies & Academics, Inc., 2019.

[12] N. Amato, Z. Huamán, A. Hyland, J. Koslow, J. Pickunka, J. Procaccini ... J. Tappen. *Design, Analysis, and Test of a High-Powered Model Rocket*. Partial Fulfillment of the Requirements for the Degree of Bachelor of Science in Aerospace Engineering, Worcester Polytechnic Institute, 2020.

[13] H. P. Kritzinger, C. R. Kleijn and H. E. A. Van den Akker. Drag on a Confined Cylinder in Axial Flow. In *ASME-PVP Symposium on Computational Technologies for Fluid/Thermal/Structural/Chemical Systems with Industrial Applications*, San Diego, CA, U.S.A., July 2004.

[14] A. Deperrois. Part IV - Theoretical limitations and shortcomings of xflr5, 2019. URL *http://www.xflr5.tech/docs/Part%20IV:%20Limitations.pdf*. (Accessed on 3-04-2022).

[15] J. M. Rainbird, J. Peiró and J. M. R. Graham. Blockage-tolerant wind tunnel measurements for a NACA 0012 at high angles of attack. *Journal of Wind Engineering and Industrial Aerodynamics, Vol. 145*, pages 209–218, 2015.

[16] D. Seter and A. Rosen. Theoretical and Experimental Study of Axial Autorotation of Simple Rotary Decelerators. *Journal of Aircraft, Vol. 51, No. 1*, pages 236–248, 2014.

[17] AeroTéc. Rocket Experiment Division, 2022. URL *https://aerotec.pt/red*. (Accessed on 8-09-2022).